ROYAL SOCIETY
OF CHEMISTRY

PAPER

Check for updates

Magnetic ordering in 45 nm-diameter multisegmented FeGa/Cu nanowires: single nanowires and arrays†

Eduardo Ortega, [ID] [a] Sai Madhukar Reddy, [ID] [b] Israel Betancourt, [c] Sina Roughani, [d] Bethanie J. H. Stadler [ID] [d] and Arturo Ponce [ID] *[a]

Magnetic nanowires are ideal candidates for many diverse applications, such as 3D magnetic memory and bio-barcodes, they also allow fundamental studies of magnetic interactions at the nanometer level. Usually their magnetic characterization involves hysteresis loops that represent the weighted averages of each entire array. Here, off-axis electron holography under Lorentz microscopy conditions has been used to observe the magnetization distribution and to determine the saturation magnetization ($M_s = 1.26 \times 10^6$ A m^{-1}) of a single 45 nm diameter FeGa(10.5 nm)/Cu(6.5 nm) nanowire. In addition, a row of segmented nanowires still within the alumina growth template was carefully sliced from the array to observe the magnetization distribution resulting from interwire as well as intersegment interactions. Two simultaneous magnetic states were observed in this novel experimental configuration: one is the antiferromagnetic ordering of segments along each wire with ferromagnetic ordering between nanowires and the second is the presence of ferromagnetic vortices along nanowire lengths. Simulations have been performed to verify the presence of both remnant states. These states demonstrate the frustration present in hexagonally packed nanowires and demonstrate the necessity to understand long range magnetic ordering for applications such as 3D magnetic memory.

Introduction

Nanoscale magnetic structures, and their ordered arrays, are being considered for use in several advanced technological areas. Analytical biosystems (*e.g.* pH, cholesterol, uric acid and protein sensors),[1–6] MEMS (*e.g.* optical, acoustic, thermo-electric sensors),[7–9] and power devices such as supercapacitors or batteries[10,11] are some of the breakthrough areas that can benefit from the control of magnetic behaviors in these tri-dimensional arrangements. Among the most promising nano-materials, high density arrays of ferromagnetic nanowires are targeted for next-generation 3D information storage in the way of barcode-like structures or spin transfer torque-based race-track memory, which relies on 3D scaling of arrays to increase information density.[12,13] These configurations differ from HAMR

(heat assisted magnetic recording) and BPM (bit patterned magnetic recording), in which they are used in hard drives which are inherently 2D and are not similar to RAM in access speed and processing.[14,15] Thus, engineering high-density arrays of ferromagnetic nanowires is among the most auspicious routes towards integrating nanostructures into magnetic architectures. Nanowires are useful structural elements because their magnetic response, behavior and interaction mechanisms are highly dependent not only upon their dimensional configuration (shape, size, and aspect ratio) but also spacing between their building elements.[16] Furthermore, nanowires can be synthesized using a range of physical and chemical methods such as: solution epitaxial, chemical vapor deposition, electrospinning, focus beam and electrodeposition.[17–20] The latter method is commonly used as it can be paired easily with porous templates to produce high aspect ratio nanowires;[21] where the alloy composition, segmentation and crystallographic texture can be adjusted by controlling the operational parameters such as voltage, pH, temperature, and the concentration of the metallic species.[22] In addition, this deposition method allows the analysis of cylindrical magnetic systems where the magnetization reversal is typically determined by the energy balance between the shape and magnetocrystalline anisotropies and by the magnetostatic interactions between segments.[23]

[a] Department of Physics and Astronomy, University of Texas at San Antonio, One UTSA Circle, San Antonio, Texas 78249, USA. E-mail: arturo.ponce@utsa.edu

[b] Chemical Engineering and Materials Science, University of Minnesota, 200 Union St. SE, Minneapolis, Minnesota 55455, USA

[c] Instituto de Investigaciones en Materiales, Universidad Nacional Autónoma de México, México City 04510, Mexico

[d] Electrical and Computer Engineering, University of Minnesota, 200 Union St. SE, Minneapolis, Minnesota 55455, USA

† Electronic supplementary information (ESI) available. See DOI: 10.1039/c7tc02314f

Iron alloys exhibit reduced crystalline anisotropy which can be easily overcome by their shape anisotropy.[24] The addition of a nonmagnetic element such as gallium (FeGa, called Galfenol) not only increases the magnetostriction of Fe in the (100) direction, but also improves its mechanical sturdiness making it an ideal material for many sensor and actuator applications.[25–27] Moreover, as a way to lower the shape anisotropy of the nanowires, or simply to stack magnetic bits, it is possible to use an intermediate non-magnetic element to segment the nanowires.[28] Although there are several research articles reported on the fabrication of FeGa nanowires and their magnetic measurements, using vibrating sample magnetometers (VSMs) or magnetic force microscopy (MFM);[28–31] only a few studies attempt to unveil the local structure/morphology of the nanowire-anodic aluminum oxide (AAO) composite and their combined effect on the composite magnetic properties.[32,33] Analyzing these systems at the nanoscale is important as traditional approaches using X-ray or VSM could overlook fine local interactions. A more focused technique, off-axis electron holography (EH), can be used to quantitatively reconstruct the 3D magnetic field configuration within ferromagnetic nanostructures to obtain local quantitative magnetic measurements to evaluate intrawire and intersegment effects.[34,35] Recently, some works have demonstrated the efficacy of using the focused ion beam (FIB) to prepare electron transparent-samples for subsequent transmission electron microscopic (TEM) examination without any detriment to the crystallinity of the samples.[33,36] The FIB can also overcome problems emerging from the permanence of an AAO capping when nanowires are etched for individual analysis. The electron beam in this type of dual-beam system has also been used for tuning the shape, composition and magnetization in individual nanowires grown using metallic gas precursors.[37] In this work, we have synthesized $Fe_{0.8}Ga_{0.2}$/Cu nanowire arrays by electrodeposition into AAO templates. Our main objective was to use electron microscopy methods for the analysis and characterization of the magnetic ordering and magnetic field distribution in multisegmented nanowires individually and, for the first time, as an array inside the template after using the FIB to obtain a single row of evenly spaced nanowires.

Experimental details

Commercially obtained (Synkera) anodized aluminum oxide (AAO) templates of a 100 nm nominal interpore distance were used as templates for electrochemical deposition of FeGa/Cu nanowires. The templates were sputter-coated with a thin adhesion layer of Ti followed by a thicker Au coating. These templates were then annealed at 200 °C in ambient air in order to improve the contact. The template was directly contacted to a rotating disk electrode using indium, followed by insulation using the Xtal bond, and it was rotated at a speed of 1800 rpm during electrodeposition. For the materials synthesis, the electrolyte consisted of $FeSO_4$ (15 mM), $Ga_2(SO_4)_3$ (17.5 mM), $CuSO_4$ (1.5 mM) and Na_3-citrate (35 mM) in DI water. The pH was adjusted to 3.75 with diluted NaOH. The counter electrode for all the electrodeposition experiments was a thin sheet of Pt foil.

Deposition potentials of −1.12 and −0.8 V vs. Ag/AgCl were used for FeGa and Cu electrodeposition, respectively. The rotating disk electrode was used to ensure growth homogeneity.

Array crystal structures were analyzed using X-ray diffraction (XRD) after polishing off the Ti/Au contact, using an Empyrean microdiffractometer (PANalytical) working at 45 kV and 40 mA with Cu-Kα radiation. Samples were prepared for TEM analysis using a Zeiss Crossbeam 340 FIB working with 30, 5 and 2 kV gallium ions; samples were also deposited on Nickel grids for regular EM analysis. High resolution TEM images were obtained on a JEOL 2010F operated at 200 kV. Electron holography and elemental composition were carried out using a JEOL ARM 200F, operated at 200 kV, equipped with an EDX detector (EDAX) both in spot analysis and line scan modes. All off-axis electron holography data acquisition was performed under Lorentz conditions, where the main objective lens is switched off, and the imaging is achieved using the objective minilens (Lorentz lens).

Results and discussion

A.   Structural characterization

The crystalline structure of the nanowires has been studied using X-ray diffraction (XRD) in a Bragg–Brentano configuration, and the X-ray pattern of the FeGa/Cu nanowires inside the AAO template is shown in Fig. 1a. The diffraction peaks correspond to the body centered cubic (bcc) $Fe_{0.8}Ga_{0.2}$, space group $Im\bar{3}m$ (ref. code 04-003-3886). This structure has been previously reported, and it has been demonstrated that slight variations in the Fe/Ga concentrations can affect the crystal system of the alloy, e.g. $Fe_{0.77}Ga_{0.23}$, $Fe_{0.75}Ga_{0.25}$ and $Fe_{0.66}Ga_{0.33}$ are arranged respectively on tetragonal, cubic and hexagonal lattices. The XRD data also show the diffraction peaks of Cu, space group $Fm\bar{3}m$. Due to the rapid decay of the FeGa signal, it is not possible to identify a preferred orientation of the crystals, probably due to the AAO volume in the array. In order to evaluate the chemical distribution and composition of the samples X-ray energy dispersive spectroscopy analysis (EDS) was used, and Fig. 1b displays a typical EDS spectrum collected over a single multisegmented nanowire together with three semi-quantitative spectra acquired along different nanowires that were removed from the AAO template by selective etching. An intense Al peak indicates that part of the AAO may be left on the nanowire after etching but the ratio of atomic percentage of Fe/Ga is around the expected value of 5. Fig. 1c shows a high-angle annular dark-field (HAADF) image obtained using scanning transmission electron microscopy (STEM) with contrast highlighting the location of the smaller Cu segments. In Fig. 1d, it is possible to observe the EDS elemental mappings of Fe, Cu and Ga. The transition between FeGa and Cu is typically cup/cone shaped which explains the count/pixel distribution among the segments. From the EDS analysis, the estimated length of the segments is 10–11 nm for Fe–Ga and 6–7 nm for Cu.

Structural analysis was performed using selected area electron diffraction (SAED) to analyze the crystallinity of the array prepared using the FIB. Electron diffraction patterns were acquired in a
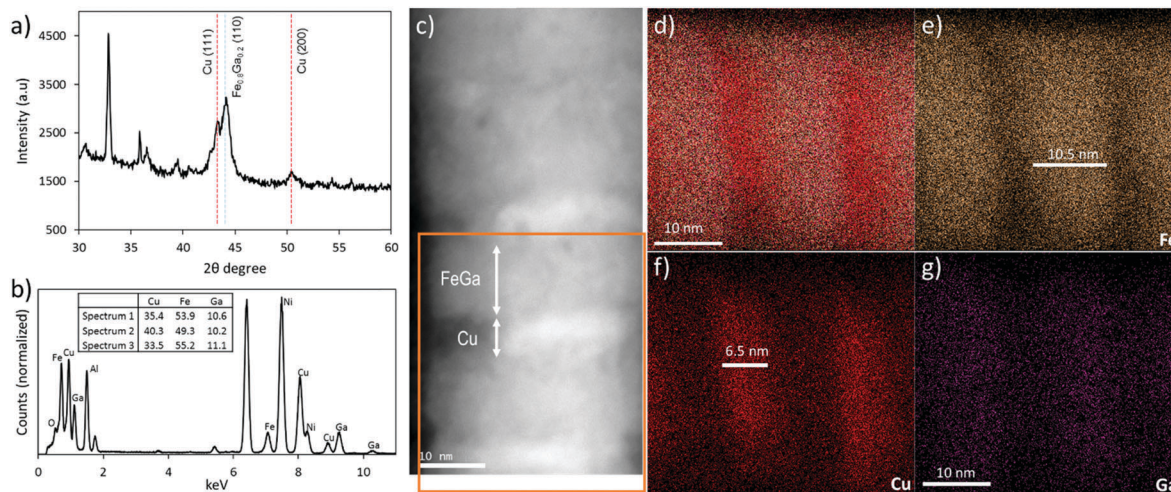
This journal is © The Royal Society of Chemistry 2017

J. Mater. Chem. C, 2017, 5, 7546–7552 | 7547

Fig. 1 XRD and EDS chemical analysis of FeGa/Cu nanowires: (a) XRD patterns of the as-prepared nanowires within the AAO template whose peaks correspond to FCC Cu and BCC FeGa. (b) EDS spectra and a table showing three semi-quantitative microanalysis results obtained from analyzing three different nanowires. (c) STEM image showing the two distinctive regions along the principal axis, the square represents the region probed for EDS mapping; (d) reveals the chemical composite of the elements of interest; EDS analysis showing the distribution of Fe (e), Cu (f) and Ga (g) along the nanowire.

250 nm diameter field of view containing evenly spaced neighboring nanowires that share the same alignment as shown in the inset in Fig. 2a. The electron diffraction patterns show a large selection of reflections attributed to the $Fe_{0.8}Ga_{0.2}$ alloy; the radial intensity profile of this pattern is presented in Fig. 2b. The segment of FeGa displays its two highest diffraction rings at 0.206 and 0.117 nm corresponding to the distance between (110) and (211) planes of the BCC structure. The presence of FCC Cu is inferred due to the appearance of rings at 0.181, 0.127 and 0.108 nm which correspond to the values for the (200), (220) and (311) Cu planes. It has been previously reported that electrochemically synthesized nanowires present a preferential orientation in the crystals along the wire axis. Pohl *et al.* demonstrated

that if a SAED pattern only has high intensity along some angular sectors of the (110) ring, it can be used as an indication of the [110] zone axis being parallel to the growth direction of the nanowires. From the SAED of the multilayered FeGa/Cu nanowires a texturized pattern was not appreciable, the homogeneous distribution of the ring intensities suggests a collection of randomly oriented crystals along the nanowires as an effect that has been produced during the pulsed deposition method of electrodeposited metallic species.[36]

High resolution TEM (HRTEM) is an imaging mode that can be used to observe in direct space the crystalline structure. FeGa/Cu polycrystalline segments of a 45 nm thick nanowire are shown in Fig. 2c. From the fast Fourier transforms (FFTs)
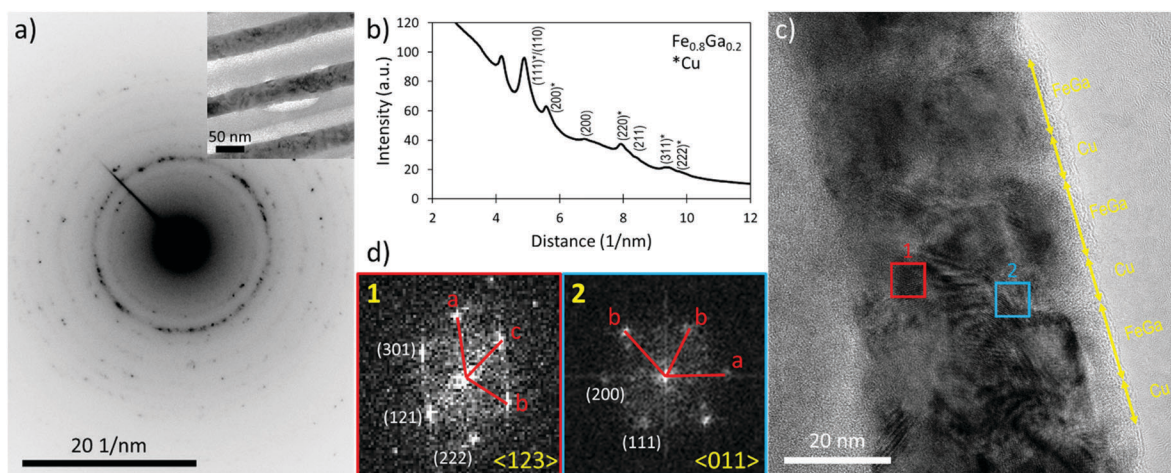
Fig. 2 Microstructure analysis of multisegmented nanowires: (a) SAED patterns of the sectioned nanowires included by the aperture and shown in the inset. (b) Rotational average intensity profile of the diffraction rings recorded in (a), the produced peaks match with the FeGa alloy, the peak around 0.180 nm is expected due to the presence of the Cu layers. (c) TEM image of a single FeGa/Cu nanowire. (d) Fourier transform of the two highlighted regions in (c), the first one corresponds to a BCC grain (FeGa) while the second points into a FCC lattice (Cu) observed through the ⟨011⟩ direction.

7548 | *J. Mater. Chem. C*, 2017, **5**, 7546–7552

This journal is © The Royal Society of Chemistry 2017

displayed in Fig. 2d, it is possible to determine the orientation parallel to the growth direction of crystallites. For example, the crystal within the box marked '1' has a–c, c–b and b–a planes at angles of 58, 76 and 46 degrees which are in close agreement with expected values of the diffraction spots of a BCC lattice observed through the ⟨123⟩ direction. Indexing this FFT, an interplanar distance of 0.085 nm for the (222) planes of the FeGa alloy can be measured. For the region marked '2' the FFT exhibited values of 53 and 74 degrees between a–b and b–b planes, which point to an FCC, for the case of Cu, lattice observed through the ⟨011⟩ direction. The presence of Moiré fringes, and the presence of dark and bright stripes suggest the overlapping of randomly aligned crystallites. This is attributed to the large lattice mismatch ($\sim$23%) between the multilayer elements and the strongly diffusion-limited growth of Cu segments affected by the alternating voltages employed during the synthesis of the nanowires.[38]

B. Magnetic characterization

To perform a reliable magnetic analysis using off-axis electron holography (EH), a single FeGa/Cu nanowire was isolated on a lacey-carbon gold grid. The holograms were recorded in a CCD camera and then analyzed using HoloWorks 5.0.7 a script within digital micrograph which allows the computation of magnetic induction and magnetic contour images. Interference fringes were oriented longitudinally in the parallel direction of the nanowire with an average fringe spacing, σ = 9.5 nm in a field of view (FOV) of 1 μm^2 and a fringe contrast of $\mu \approx$ 40%. In order to obtain quantitative data from a single nanowire, the magnetic phase was separated by performing *in situ* magnetic reversal and image processing using the holograms before and after the *in situ* magnetization. In a previous work, we reported the external magnetic field produced by the objective lens of the microscope used, the JEOL ARM 200F, which can reach a value of 1.8 T when the objective lens is saturated at 10 V.[39] The *in situ* magnetization process is performed by tilting the sample (positive and negative angles, to reverse the magnetization) and turning on momentarily the objective lens, then the sample is tilted back to the original position to collect the holograms.[40] In this experiment, after the nanowire was tilted $\pm$22°, a **H** field of 1.8 T was applied perpendicular to the specimen stage (Fig. S1, ESI†). The parallel component of the **H** field acting along the nanowire axis is in the order of 7.2 T which is well over the saturation field **H**$_s$ of 2.5 T necessary to reach the saturation magnetization of the nanowires, as reported in the literature.[41,42] The electrostatic contribution (Fig. 3b) is obtained from half the sum of the holograms obtained after the magnetization procedure, while the pure magnetic phase contribution (Fig. 3c) is obtained from half their difference. Fig. 3d is obtained by superimposing the values of the magnetic induction and the three times amplified unwrapped magnetostatic contribution, these contours have a direct correspondence with the magnetic flux lines of the nanowire, and the color wheel inset indicates the flux directions going mainly through the nanowire axis. This axial orientation clearly reflects the predominant influence of the shape anisotropy (favoring longitudinal direction) over the vanishing
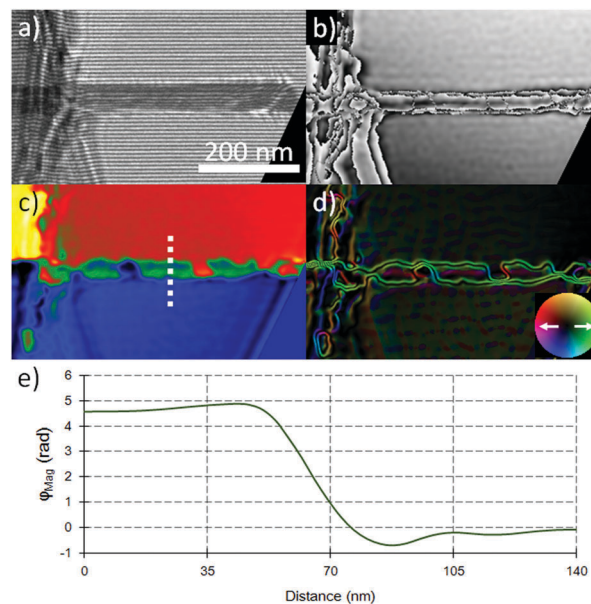

Fig. 3 (a) Electron hologram of a single segmented FeGa/Cu nanowire. (b) Amplification of the unwrapped electrostatic and (c) magnetic contribution. (d) Amplification of the magnetic contour, lines represent the magnetic flux passing through the nanowire axis. (e) Phase shift across the dashed line in the magnetic phase image in (c).

magnetocrystalline anisotropy as expected from micromagnetic simulations. At the longitudinal edges of the nanowire, the magnetic flux exhibits a wavy pattern, associated with fringing fields at the magnetic/diamagnetic interface of the FeGa/Cu segments. At the tip of the nanowire (on the right-hand side of Fig. 3d), the closure of flux lines resembles a vortex structure, which prevents flux leakage and is a minimization of magnetostatic energy as observed in a previous experimental work reported by Rodriguez *et al.*[43] In addition, some voids are visible as black zones along the nanowire axis, which might be indicative of a change of the magnetic flux orientation, from the axial to perpendicular direction, due to demagnetizing effects for energy minimization as it will be emphasized in the next micromagnetic simulations. The magnetic phase profile across the nanowire is plotted in Fig. 3e, and it corresponds to the observed phase shift, as expected from the magnetic induction within the nanowire. A quantitative value of the magnetic flux can be obtained from the reconstructed phase maps, different researchers have worked on similar experimental calculations which depend on both the total phase shift ($\Delta\varphi$) across the nanowire and geometrical parameters (Fig. S2, ESI†).[44] The magnetization and magnetic induction were quantitatively evaluated as $M = 1.26 \times 10^6$ A m^{-1} and $B = 1.58$ T from the total phase shift of 5.3 rad for the nanowire shown in Fig. 3a with a diameter of 43 nm, this is consistent with experimental B values between 1.52 and 1.63 T reported for bulk Fe$_{80}$Ga$_{20}$ alloys.[26,27]

A micromagnetic simulation based on the experimental structure has been performed for an ideal, well-defined nanowire structure (see details of the method in Fig. S3 and S4, ESI†).[45] There is a good agreement between simulations and experimental observations, since most of the magnetic flux

presents an axial orientation, reflecting the prevalent influence of the shape anisotropy. The longitudinal configuration includes several FeGa segments with mostly axial orientation with some wavy patterns, also present in the magnetic flux image (Fig. 3d), from transitions between FeGa segments having a perpendicular orientation. Out-of-axis oriented FeGa portions are symmetrically distributed along the longitudinal edges (some examples are circled in Fig. 4). At the nanowire main axis, the longitudinal direction is more pronounced, favored also by the exchange coupling interaction, which defines axial orientation for minimization of energy. The role of the diamagnetic Cu-segments is to facilitate the reorientation of the magnetic flux between FeGa/Cu segments. In addition, a vortex-like structure appears at the tips of both the experimental and simulated images, which facilitates the minimization of flux leakage attaining a minimum of magnetostatic energy. According to our micromagnetic calculations, the observed vortex structure does not propagate because of the magnetization reversal but rather a local coherent rotation mechanism begins at the interface FeGa/Cu layers, completing first the reorientation of magnetization at the axially oriented areas, followed by a progressive rotation of the perpendicular zones towards the nanowire main axis. The vortex structure progressively vanishes as the spin rotation completes magnetic saturation in the opposite direction.

As a way to visualize the effect of neighboring nanowires, the in-plane component of magnetic induction inside a nanowire array within the alumina template was imaged using EH. For reference, Fig. 5a shows the TEM image of a section of the array prepared with the FIB to obtain an electron-transparent row of multisegmented nanowires. The holograms were acquired under Lorentz conditions with the same settings (FOV, σ, and μ) as those used for the single nanowire phase reconstruction shown in Fig. 3. In the array of nanowires, the magnetic phase separation was carried out by recording holograms of the same FOV at two different accelerating voltages (200 kV and 120 kV). Once the two holograms are acquired, a substitution method is performed to eliminate the crystalline potential contribution from the unwrapped phase images. Following this separation method, the magnetization behavior retrieved is perpendicular to the longitudinal axis of the nanowires, induced by the external magnetic field produced by the objective lens.[37] The detailed method to separate the magnetic phase contribution is available in the Fig. S5, ESI.† The magnetic induction image shown in Fig. 5b is obtained from the phase gradient and weighted amplitude from the magnetic contribution phase image.

A TEM image of the arrays of nanowires is used to identify locally the magnetic arrangement obtained using electron holography, shown in Fig. 5a and b, respectively. The cross interaction of neighboring nanowires when they are close

Fig. 4 Calculated remnant state for the cylindrical FeGa/Cu model. The longitudinal section was taken at the middle of the cylinder. Circled areas indicate examples of magnetization with perpendicular direction (relative to longitudinal axis).

Fig. 5 (a) TEM image of the nanowire array used for EH. (b) Magnetic induction image reconstructed from holograms taken at different accelerating voltages, showing AFM intersegment/FM interwire order (alternating green/magenta in NW 2–5) and FM vortices (cyan/orange longitudinal edges in NWs 7, 9–11). (c) OOMMF simulation where dimensions and distribution of the nanowires from image (b) were modeled. The row was saturated perpendicular to the nanowire axes and then the structure returned to a remnant state that had the same two simultaneous states of order as those in (b).

enough (solid square) does not occur with more spaced alumina template columns, marked in the solid line between the nanowires 8 and 9 of Fig. 5a. Nanowire number 2 lacks the Cu segments (solid circle) which shows a stacking of disks with alternating magnetization values as indicated compared with the nanowire 4 (dash line) in which a different magnetic behavior occurs as indicated in the color wheel of Fig. 5b.

In nanowires in the lower left corner (nanowires 2–4, parts of 5), antiferromagnetic (AFM) coupling is observed where the color wheel shows opposing colors as magenta and light green in the direction perpendicular to the nanowire axes. These directions show remnant magnetization lying in the plane of the pancake-shaped FeGa segments with AFM coupling between segments, and the coupling between adjacent nanowires is mostly ferromagnetic (FM), but not strictly so. In the upper right corner (nanowires 7, 9–11), the orange-cyan coloring along the edges of the nanowires is indicative of vortices that have a canting along the nanowire axes. Vortices are structures with closed flux, and the TEM image shows both the "front" and "back" of the vortex, so the nanowires appear darker in the induction images as signals cancel, except for the small edge effect seen. Both states of order were observed in object oriented micromagnetic framework (OOMMF) simulations (Fig. 5c) when the nanowires were saturated perpendicular to their axes and then allowed to relax to a remnant state. The vortex domain wall exhibited in the array is consistent with the magnetic properties measured in the template using vibrating sample magnetometry (VSM) (Fig. S6, ESI†).[35]

Conclusions

In summary, off-axis EH methods have been used to visualize the magnetic flux in electrodeposited $Fe_{0.8}Ga_{0.2}$/Cu multisegmented nanowires where the favored longitudinal orientation was confirmed using EH and micromagnetic simulations; the nanowires were found to have saturation magnetization in close agreement with their bulk counterpart. In addition, electron holograms allowed us to visualize the magnetic induction in a row of nanowires to see the effect between neighboring nanowires. In the case where the ensemble was saturated perpendicular to the nanowire axes two states of order were observed: AFM intersegment/FM interwire ordering and a FM vortex ordering, the same behavior was also found in OOMMF simulations within the same parameters. These results have a significant impact on the field of high density 3D memory as the magnetic segments observed here will be entangled together in ordered structures that may hinder desired configurations where a single nanowire in a high-density packed array can function as an individual and unperturbed information bit. We are therefore able to visualize and demonstrate a limit to the density of individual bits in 3D memory.

Acknowledgements

References

1 K. M. Pondman, A. W. Maijenburg, F. B. Celikkol, A. A. Pathan, U. Kishore, B. ten Haken and J. E. ten Elshof, *J. Mater. Chem. B*, 2013, **1**, 6129.

2 A. Nehra and K. Pal Singh, *Biosens. Bioelectron.*, 2015, **74**, 731–743.

3 Y.-M. Chu, C.-C. Lin, H.-C. Chang, C. Li and C. Guo, *Biosens. Bioelectron.*, 2011, **26**, 2334–2340.

4 R. Ahmad, N. Tripathy and Y.-B. Hahn, *Biosens. Bioelectron.*, 2013, **45**, 281–286.

5 X. Liu, P. Lin, X. Yan, Z. Kang, Y. Zhao, Y. Lei, C. Li, H. Du and Y. Zhang, *Sens. Actuators, B*, 2013, **176**, 22–27.

6 Y. Ohno, K. Maehashi and K. Matsumoto, *Biosens. Bioelectron.*, 2010, **26**, 1727–1730.

7 Y. Su, M. Gao, X. Meng, Y. Q. Chen, Q. T. Zhou, L. Li and Y. Feng, *J. Phys. Chem. Solids*, 2009, **70**, 1062–1065.

8 P. D. McGary, L. Tan, J. Zou, B. J. H. Stadler, P. R. Downey and A. B. Flatau, *J. Appl. Phys.*, 2006, **99**, 08B310.

9 M. L. Wierzbicki, J. Barna and R. Swirkowicz, *J. Phys.: Condens. Matter*, 2015, **27**, 485301.

10 F. Hekmat, B. Sohrabi, M. S. Rahmanifar and M. R. Vaezi, *J. Mater. Chem. A*, 2014, **2**, 17446–17453.

11 S. Demirel, E. Oz, E. Altin, S. Altin, a. Bayri, P. Kaya, S. Turan and S. Avci, *Mater. Charact.*, 2015, **105**, 104–112.

12 T. Shimizu, K. Aoki, Y. Tanaka, T. Terui and S. Shingubara, *Jpn. J. Appl. Phys.*, 2011, **50**, 06GE01.

13 E. Cisternas and E. E. Vogel, *J. Magn. Magn. Mater.*, 2015, **388**, 35–39.

14 Z. Meng, G. Li, S.-M. Ng, H.-F. Wong, S.-C. Yiu, C.-L. Ho, C.-W. Leung and W.-Y. Wong, *Polym. Chem.*, 2016, **7**, 4467–4475.

15 Z. Meng, G. Li, H.-F. Wong, S. M. Ng, S.-C. Yiu, W.-Y. (Raymond) Wong, C.-L. Ho, C. W. Leung and I. Manners, *Nanoscale*, 2017, **9**, 731–738.

16 R. P. Cowburn, *J. Phys. D: Appl. Phys.*, 1999, **33**, R1–R16.

17 Y. Li, C. Cao and Z. Chen, *J. Phys. Chem. C*, 2010, **114**, 21029–21034.

18 T. Moon, W.-Y. Lee, C.-J. Choi and J.-W. Yoon, *Appl. Phys. Lett.*, 2014, **105**, 153103.

19 L. A. Rodríguez, L. Deen, R. Córdoba, C. Magén, E. Snoeck, B. Koopmans and J. M. De Teresa, *Beilstein J. Nanotechnol.*, 2015, **6**, 1319–1331.

20 A. Fert and L. Piraux, *J. Magn. Magn. Mater.*, 1999, **200**, 338–358.

This journal is © The Royal Society of Chemistry 2017

J. Mater. Chem. C, 2017, **5**, 7546–7552 | 7551

21 G. W. Meng, A. Y. Cao, J. Y. Cheng, A. Vijayaraghavan, Y. J. Jung, M. Shima and P. M. Ajayan, *J. Appl. Phys.*, 2005, **97**, 064303.

22 A. S. Esmaeily, M. Venkatesan, A. S. Razavian and J. M. D. Coey, *J. Appl. Phys.*, 2013, **113**, 1–4.

23 K. Ounadjela, R. Ferre, L. Louail, J. M. George, J. L. Maurice, L. Piraux and S. Dubois, *J. Appl. Phys.*, 1997, **81**, 5455–5457.

24 C. Bran, Y. P. Ivanov, J. García, R. P. del Real, V. M. Prida, O. Chubykalo-Fesenko and M. Vazquez, *J. Appl. Phys.*, 2013, **114**, 43908.

25 E. C. Estrine, M. Hein, W. P. Robbins and B. J. H. Stadler, *J. Appl. Phys.*, 2014, **115**, 17A918.

26 A. E. Clark, M. Wun-Fogle, J. B. Restorff and T. A. Lograsso, *Mater. Trans., JIM*, 2002, **43**, 881–886.

27 D. Iselt, U. Gaitzsch, S. Oswald, S. Fahler, L. Schultz and H. Schlorb, *Electrochim. Acta*, 2011, **56**, 5178–5183.

28 J. Jin Park, M. Reddy, C. Mudivarthi, P. R. Downey, B. J. H. Stadler and A. B. Flatau, *J. Appl. Phys.*, 2010, **107**, 09A954.

29 J. Jin Park, M. Reddy, B. J. H. Stadler and A. B. Flatau, *J. Appl. Phys.*, 2013, **113**, 17A331.

30 S. Vock, K. Tschulik, M. Uhlemann, C. Hengst, S. Fähler, L. Schultz and V. Neu, *J. Appl. Phys.*, 2015, **118**, 233901.

31 J. Battogtokh, S. Kang, Y. Chao, M. J. Wagner, M. Brandys, A. C. Buechele, I. L. Pegg and J. Philip, *J. Appl. Phys.*, 2009, **105**, 07A933.

32 Y. P. Ivanov, D. G. Trabada, A. Chuvilin, J. Kosel, O. Chubykalo-Fesenko and M. Vázquez, *Nanotechnology*, 2014, **25**, 475702.

33 B. Rodríguez-González, C. Bran, T. Warnatz, J. Rivas and M. Vazquez, *J. Appl. Phys.*, 2014, **115**, 133904.

34 D. Wolf, L. A. Rodriguez, A. Béché, E. Javon, L. Serrano, C. Magen, C. Gatel, A. Lubk, H. Lichte, S. Bals, G. Van Tendeloo, A. Fernández-Pacheco, J. M. De Teresa and E. Snoeck, *Chem. Mater.*, 2015, **27**, 6771–6778.

35 D. Reyes, N. Biziere, B. Warot-Fonrose, T. Wade and C. Gatel, *Nano Lett.*, 2016, **16**, 1230–1236.

36 D. Pohl, C. Damm, D. Pohl, L. Schultz and H. Schlörb, *Nanotechnology*, 2016, **27**, 35705.

37 J. Pablo-Navarro, D. Sanz-Hernández, C. Magén, A. Fernández-Pacheco and J. M. de Teresa, *J. Phys. D: Appl. Phys.*, 2017, **50**, 18LT01.

38 S. M. Reddy, J. J. Park, S. M. Na, M. M. Maqableh, A. B. Flatau and B. J. H. Stadler, *Adv. Funct. Mater.*, 2011, **21**, 4677–4683.

39 J. Cantu-Valle, F. Ruiz-Zepeda, F. Mendoza-Santoyo, M. Jose-Yacaman and A. Ponce, *Ultramicroscopy*, 2014, **147**, 44–50.

40 J. Cantu-Valle, I. Betancourt, J. E. Sanchez, F. Ruiz-Zepeda, M. M. Maqableh, F. Mendoza-Santoyo, B. J. H. Stadler and A. Ponce, *J. Appl. Phys.*, 2015, **118**, 24302.

41 L. A. Rodríguez, C. Magén, E. Snoeck, C. Gatel, L. Marín, L. Serrano-Ramón, J. L. Prieto, M. Muñoz, P. A. Algarabel, L. Morellon, J. M. De Teresa and M. R. Ibarra, *Ultramicroscopy*, 2013, **134**, 144–154.

42 S. Madhukar Reddy, J. Jin Park, M. M. Maqableh, A. B. Flatau and B. J. H. Stadler, *J. Appl. Phys.*, 2012, **111**, 07A920.

43 L. A. Rodríguez, C. Bran, D. Reyes, E. Berganza, M. Vázquez, C. Gatel, E. Snoeck and A. Asenjo, *ACS Nano*, 2016, **10**, 9669–9678.

44 C. Beeli, B. Doudin and P. Stadelmann, *Phys. Rev. Lett.*, 1995, **75**, 4630–4633.

45 J. Fidler and T. Schrefl, *J. Phys. D: Appl. Phys.*, 2000, **33**, R135–R156.